Journal of Thermal Science and Engineering Applications. Received November 14, 2025;
Accepted manuscript posted March 31, 2026. doi:10.1115/1.4071557

Computational investigation of the cooling and heating effect in vortex tube

Dingli Duan[1], Shuaibing Guan[1], Yanfeng Qiao[2], Jay Wang[3*]

1 Department of Thermal Energy and Power Engineering, Yantai University, Yantai, China

2 Wanhua Chemical(yantai) Chlor-alkali Thermal Power Co., Ltd., Yantai, China

3 School of Engineering, Computer & Mathematical Sciences, Auckland University of Technology (AUT), Auckland, New Zealand

Corresponding Author: Jay Wang, Email: jay.wang@aut.ac.nz

ABSTRACT

Vortex tubes exhibit a unique temperature separation phenomenon, leading to their widespread application in refrigeration and heating. Using the exact flow and temperature field simulation, this study examined the cooling effect and heating effect under different cold mass fractions, inlet pressure and diameter ratios. The cooling effect shows a trend of first increasing and then decreasing with the increase of the cold mass fractions while the heating effect gradually increases. Actually, the cooling and heating effect are suppressed by backflow, it is difficult for the working fluid to flow out of the cold end leading to the backflow at the cold end is severe at low cold mass fractions, and the reverse flow boundary exceeds the control valve causing the backflow at the hot exit is enhanced at high cold mass fractions. In order to get excellent cooling effect and heating effect of the vortex tube, the inlet pressure should be increased while reducing the diameter ratio of the vortex tube, and the cold mass fractions should be controlled within a reasonable range (CMF=0.3~0.7).

Key words: vortex tube; turbulence model; cold mass fraction; cooling effect; heating effect

Nomenclature	
c_p	specific heat capacity at constant pressure [J kg^{-1} K^{-1}]
H	enthalpy [kJ/kg]

m	mass flow rate [kg/s]
p	pressure [Pa]
R	the ideal gas constant
T	temperature [K]
u	velocity [m/s]
U_z	the axial velocity in z direction[m/s]
Abbreviations	
CMF	cold mass fraction
DR	diameter ratio
LES	large eddy simulation
RSM	Reynolds–Stress model
SA	Spalart–Allmaras

1. Introduction

Due to the absence of mechanical motion components within the vortex tube, the energy drive unit is unnecessary during operation, the service cycle is long, and it is easy to maintain and manage. As a result, it has substantial research significance and uses for energy conservation and environmental protection[1,2]. As an energy and mass separator, vortex tube plays a vital role in cooling[3,4], heating[5,6], drying[7] and seawater desalination[8].

Vortex tubes combine tangential inlet, cold end, and hot exit into one main pipe[9]. There are usually different numbers of tangential inlets in vortex tubes, and the number of tangential inlets is generally even[10]. Cold end and tangential inlet are located closer to each other than hot exit, while hot exit is equipped with a control valve to regulate the mass flow from cold end to hot exit[11]. High pressure fluid rushes into the vortex tube from the tangential inlets, creating a strong swirling flow due to wall constraints and resulting in a unique temperature separation phenomenon[12,13]. Consequently, the hot fluid discharges the hot end, while the cold fluid discharges the cold end. This results in a cooling effect at the cold end and a heating effect at the hot

exit, as a result, vortex tubes are widely used in refrigeration and heating applications.

However, the vast majority of research on vortex tubes focuses on the energy separation mechanism[14,15]. In fact, the cooling effect and heating capability generated by the energy separation phenomenon are the main basis for determining the application of vortex tubes. Therefore, it is necessary to conduct a detailed study on the cooling effect and heating capability of vortex tubes.

Cooling effect and heating capability in vortex tubes is closely related to the complex and variable strong swirling flow, and it is challenging to obtain the flow pattern and flow field structure of strong swirling flow through theoretical calculations and experimental investigations. It is difficult to clarify the influence of the flow pattern and flow field structure of a strong swirling flow on the cooling effect and heating capability. As computer technology has advanced in recent decades, numerical simulation has gradually gained popularity. By using numerical simulations, one can obtain abundant study results in a short period of time, as well as better depict the flow patterns and flow field structures of a strong swirling flow[16]. Numerical simulations have become an important means of studying the cooling effect and heating capability of the vortex tube, providing more opportunities for its development and application.

Common turbulence models used in the vortex tube include Spalart–Allmaras(SA), κ–ε, κ–ω, Reynolds–Stress model(RSM) and large eddy simulation (LES), however, one turbulence model was selected by the majority study[17,18]. Only a few scholars have adopted comparative studies of multiple turbulence models to study the temperature separation in vortex tubes. The comparison on different turbulence models used in the vortex tube is given in **Table 1**. Based on the analysis of the below literature, it can be concluded that despite several models being used to simulate the vortex tube, no widely accepted turbulence model is currently available, the two models: standard κ–ε and SST κ–ω have been proven to be good choices for studying cooling and heating effect in vortex tubes.

Table 1 Comparison of different turbulence model adopted in the vortex tube

Investigator	Turbulence Model	Recommendation

Thakare and Parekh[19]	SA standard κ–ε standard κ–ω	SA
Bianco et al.[20]	standard κ–ε RSM LES	RSM
Baghdad et al.[21]	κ–ε κ–ω SST κ–ω RSM	RSM
Liu and Liu[22]	standard κ–ε RNG κ–ε realizable κ–ε SST κ–ω RSM	RSM realizable κ–ε
Awan et al.[23]	κ–ε κ–ω SST κ–ω SAS–SST	κ–ε
Shaji et al.[24]	standard κ–ε realizable κ–ε RNG κ–ε SST κ–ω	RNG κ–ε
Wang and Suen[25]	standard κ–ε RNG κ–ε standard κ–ω SST κ–ω	standard κ–ε SST κ–ω
Dutta et al.[26]	standard κ–ε RNG κ–ε	standard κ–ε

Hu et al.[27]	standard κ–ω SST κ–ω standard κ–ε RNG κ–ε standard κ-ω RNG κ–ε	standard κ–ε
Tang et al.[28]	standard κ–ε standard κ–ω RSM	standard κ–ε
Chen et al.[29]	standard κ–ε standard κ–ω RNG κ–ε RSM	standard κ–ε
Liang et al.[30]	standard κ–ε RNG κ–ε realizable κ–ε standard κ–ω SST κ–ω	SST κ–ω
Oberti et al.[31]	standard κ–ε SST κ–ω	SST κ–ω

The reason there isn't a precise model that can effectively analyze the energy separation of a vortex tube is because researchers ignore the flow patterns and flow field structures of complex strong swirling inside the vortex tube and compare temperature directly between the numerical data and experimental results. The correct method is to compare the flow characteristics obtained from numerical simulations with the flow structure obtained from experiments. Only after verifying the accuracy of the numerical simulations can further comparison and analysis of the temperature field be conducted.

Therefore, the objective of this present research is to obtain a turbulence model

that best reflects the flow and temperature separation inside the vortex tube, and to analyze the cooling and heating effects of the vortex tube under different cold mass fractions, inlet pressure, and diameter ratios, in order to contribute to the expansion of the application of vortex tubes.

2. Computational model

2.1 Physical model of the vortex tube

The geometric model of the vortex tube carried out in this numerical simulation is the same as Guo et al[32]. A schematic of this vortex tube is shown in **Fig. 1(a)**, and the geometrical parameters of this vortex tube calculated using Computational Fluid Dynamics are also listed in **Fig. 1(b)**. There are four tangential inlet nozzles in the main pipe, and the diameter of each inlet nozzle is 1.5 mm. The diameter of the cold end D_c is 15 mm, the diameter of the main pipe D_m is 30 mm, and the length of the main pipe L_m is 360 mm. The diameter ratio (DR) is defined the ratio of the diameter of the cold end D_c to the diameter of the of the main pipe D_m.

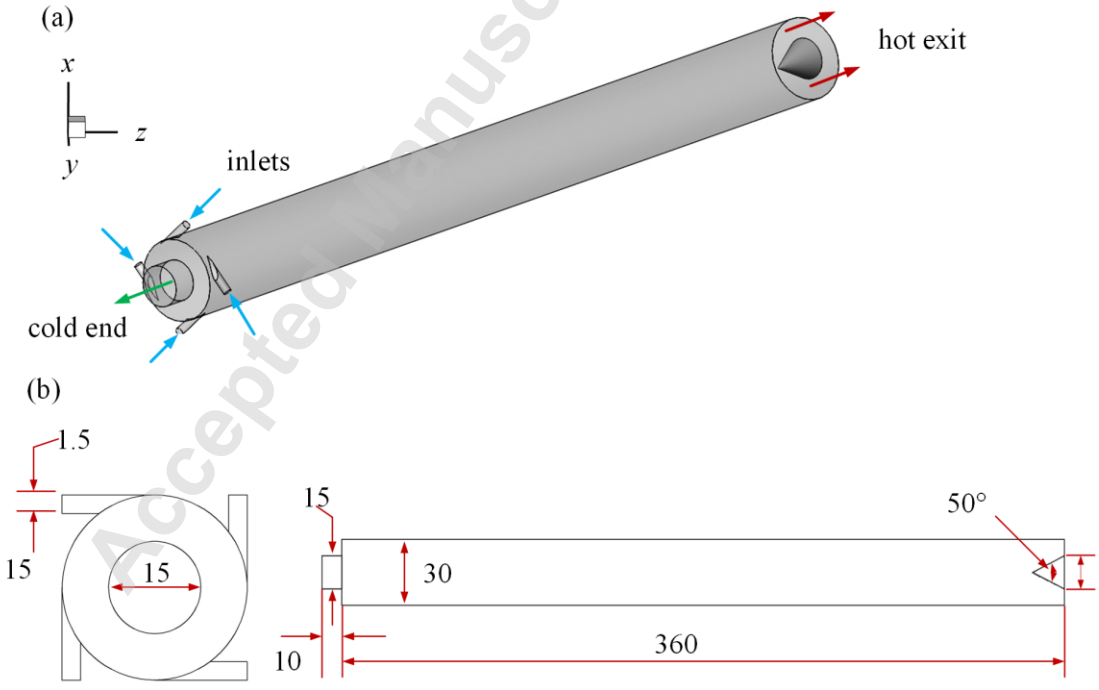

Fig. 1 (a) 3D model of the vortex tube; (b) Geometrical parameters of this vortex tube

2.2 Governing equations and turbulence models

As the working fluid, high-pressure air was chosen, and it was considered to be an ideal gas. According to the equations of mass conservation, momentum conservation, energy conservation, and ideal gas state for this vortex tube of high pressure, the following equations were solved:

Mass conservation equation:

$$\frac{\partial \rho}{\partial t}+\frac{\partial}{\partial x_i}\left(\rho \overline{u_i}\right)=0 \tag{1}$$

Momentum conservation equation:

$$\frac{\partial}{\partial t}\left(\rho \overline{u_i}\right)+\frac{\partial}{\partial x_i}\left(\rho \overline{u_i u_j}\right)=\frac{\partial}{\partial x_j}\left(\mu \frac{\partial \overline{u_i}}{\partial x_j}-\rho \overline{u_i' u_j'}\right)-\frac{\partial p}{\partial x_i} \tag{2}$$

Energy conservation equation:

$$\frac{\partial}{\partial \mathrm{t}}(\rho H)+\frac{\partial}{\partial x_i}\left(\rho \overline{u_j} H\right)=\frac{\partial p}{\partial t}+\frac{\partial}{\partial x_j}\left(\frac{\kappa}{c_{\mathrm{p}}} \frac{\partial H}{\partial x_j}-\rho \overline{u_i' H}\right) \tag{3}$$

Ideal gas state equation:

$$p=\rho R T \tag{4}$$

where ρ is the density of ideal gas; u is the velocity of ideal gas; p is the static pressure of ideal gas; H is the total enthalpy of ideal gas; κ is the thermal conductivity of ideal gas; c_{p} is the specific heat capacity at constant pressure of ideal gas; R is the ideal gas constant; and T is the temperature of the ideal gas. In the present numerical simulations, the detailed transport equation of used each turbulence model is given in **Table 2**.

Table 2 Turbulence models and transport equation used in this study

Turbulence model	Transport equation
SA	$\frac{\partial}{\partial t}(\rho \nu)+\frac{\partial}{\partial x_i}(\rho \nu u_i)=G_\nu+\frac{1}{\sigma_\nu}\left[\frac{\partial}{\partial x_j}\left\{(\mu+\rho \nu)\frac{\partial \nu}{\partial x_j}\right\}+C_{b2}\rho\left(\frac{\partial \nu}{\partial x_j}\right)^2\right]-Y_\nu+S_\nu$
standard κ–ε	$\frac{\partial}{\partial t}(\rho \kappa)+\frac{\partial}{\partial x_i}(\rho \kappa u_i)=\frac{\partial}{\partial x_j}\left[\left(\mu+\frac{\mu_t}{\sigma_\kappa}\right)\frac{\partial \kappa}{\partial x_j}\right]+G_\kappa+G_b-\rho\varepsilon-Y_M+S_\kappa$

$$\frac{\partial}{\partial t}(\rho\varepsilon)+\frac{\partial}{\partial x_i}(\rho\varepsilon u_i)=$$

$$\frac{\partial}{\partial x_j}\left[\left(\mu+\frac{\mu_t}{\sigma_\varepsilon}\right)\frac{\partial\varepsilon}{\partial x_j}\right]+C_{1\varepsilon}\frac{\varepsilon}{\kappa}\left(G_\kappa+C_{3\varepsilon}G_b\right)-C_{2\varepsilon}\rho\frac{\varepsilon^2}{\kappa}+S_\varepsilon$$

$$\frac{\partial}{\partial t}(\rho\kappa)+\frac{\partial}{\partial x_i}(\rho\kappa u_i)=\frac{\partial}{\partial x_j}\left[\alpha_\kappa\mu_{eff}\frac{\partial\kappa}{\partial x_j}\right]+G_\kappa+G_b-\rho\varepsilon-Y_M+S_\kappa$$

RNG κ–ε

$$\frac{\partial}{\partial t}(\rho\varepsilon)+\frac{\partial}{\partial x_i}(\rho\varepsilon u_i)=$$

$$\frac{\partial}{\partial x_j}\left[\alpha_\varepsilon\mu_{eff}\frac{\partial\varepsilon}{\partial x_j}\right]+C_{1\varepsilon}\frac{\varepsilon}{\kappa}\left(G_\kappa+C_{3\varepsilon}G_b\right)-C_{2\varepsilon}\rho\frac{\varepsilon^2}{\kappa}-R_\varepsilon+S_\varepsilon$$

$$\frac{\partial}{\partial t}(\rho\kappa)+\frac{\partial}{\partial x_i}(\rho\kappa u_i)=\frac{\partial}{\partial x_j}\left[\Gamma_\kappa\frac{\partial\kappa}{\partial x_j}\right]+G_\kappa-Y_\kappa+S_\kappa$$

standard κ–ω

$$\frac{\partial}{\partial t}(\rho\omega)+\frac{\partial}{\partial x_i}(\rho\omega u_i)=\frac{\partial}{\partial x_j}\left[\Gamma_\omega\frac{\partial\omega}{\partial x_j}\right]+G_\omega-Y_\omega+S_\omega$$

$$\frac{\partial}{\partial t}(\rho\kappa)+\frac{\partial}{\partial x_i}(\rho\kappa u_i)=\frac{\partial}{\partial x_j}\left[\Gamma_\kappa\frac{\partial\kappa}{\partial x_j}\right]+G_\kappa-Y_\kappa+S_\kappa$$

SST κ–ω

$$\frac{\partial}{\partial t}(\rho\omega)+\frac{\partial}{\partial x_j}(\rho\omega u_j)=\frac{\partial}{\partial x_j}\left[\Gamma_\omega\frac{\partial\omega}{\partial x_j}\right]+G_\omega-Y_\omega+D_\omega+S_\omega$$

RSM

$$\frac{\partial}{\partial t}\left(\rho\overline{u_i'u_j'}\right)+\frac{\partial}{\partial x_\kappa}\left(\rho u_\kappa\overline{u_i'u_j'}\right)=$$

$$-\frac{\partial}{\partial x_\kappa}\left[\rho\overline{u_i'u_j'u_\kappa'}+\overline{p'\left(\delta_{\kappa j}u_i'+\delta_{i\kappa}u_j'\right)}\right]$$

$$+\frac{\partial}{\partial x_\kappa}\left[\mu\frac{\partial}{\partial x_\kappa}\left(\overline{u_i'u_j'}\right)\right]-\rho\left(\overline{u_i'u_\kappa'}\frac{\partial u_j}{\partial x_\kappa}+\overline{u_j'u_\kappa'}\frac{\partial u_i}{\partial x_\kappa}\right)$$

$$-\rho\beta\left(g_i\overline{u_j'\theta}+g_j\overline{u_i'\theta}\right)+p'\left(\frac{\partial u_i'}{\partial x_j}+\frac{\partial u_j'}{\partial x_i}\right)$$

$$-2\mu\overline{\frac{\partial u_i'}{\partial x_\kappa}\frac{\partial u_j'}{\partial x_\kappa}}-2\rho\Omega_\kappa\left(\overline{u_j'u_m'}\varepsilon_{i\kappa m}+\overline{u_i'u_m'}\varepsilon_{j\kappa m}\right)+S$$

2.3 Grid generation and validation

The ANSYS ICEM CFD was used in this study to deal with the vortex tube and

obtain different numbers of mesh, and the mesh is predominantly structured with a localized geometric transition zone at the cone tip. The grid quality meets numerical simulation requirements, and the grid details at the tangential inlet, main pipe, and hot exit are shown in **Fig. 2**. Grid refinement has been carried out at the tangential inlet, cold end and hot end exit. The mesh employed for hot exit is dominated by quadrilateral structured grids. Owing to the geometric particularity of the cone tip, a smooth transition from quadrilateral grids to triangular grids is implemented at the tip zone, relying on the structured body-fitted topological features of the O-grid and realize the transition via structured topology with shared edges and nodes. The main objective of this design is to ensure the orthogonality and regularity of the mesh, fundamentally avoid problems of high skewness and non-orthogonality, and thus guarantee the accuracy and stability of the CFD calculation results. Seven different cell numbers were established for one vortex tube model to validate grid independence, the temperature difference between the hot exit and cold end, referred to as ΔT, was used for grid independence verification is displayed in **Table 3**. It can be clearly seen that the temperature difference between the hot exit and cold end ΔT shows a trend of first increasing significantly and then remaining basically unchanged with the increase of the cell number. Therefore, when the number of grids is 481520, numerical simulation can ensure accuracy and save computing resources as much as possible.

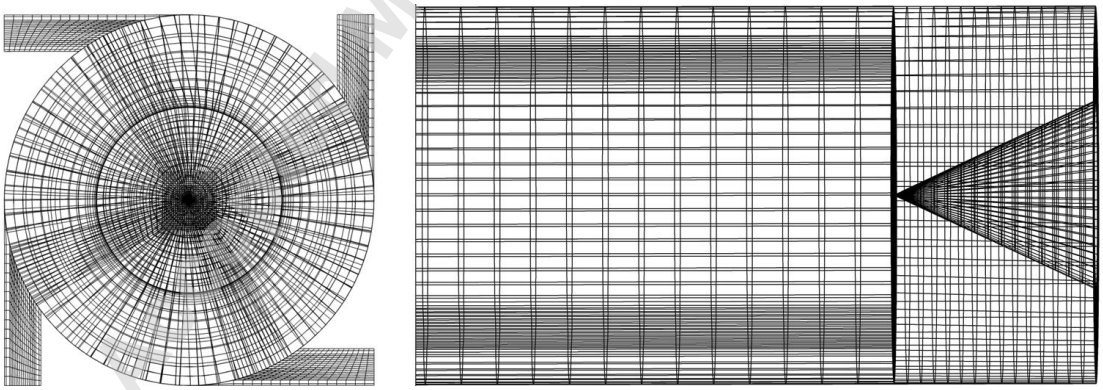

Fig. 2 Grid details of this vortex tube

Table 3 Verification of grid independence in numerical simulation of vortex tubes

Cell numbers	ΔT/K	Error/%
95720	1.5	71.2%

188490	2	61.5%
294850	3.1	40.4%
376460	4	23.1%
481520	5.1	2%
590310	5.2	0
689240	5.2	0

2.4 Boundary conditions and computational method

To ensure that the comparison between numerical simulation data and experimental research results is accurate, the boundary conditions of numerical simulation should be consistent with the actual working conditions of experimental research [32] is valuable and can reduce errors. The corresponding conditions were listed in **Table 4**. The temperature was set as 293 K, the inlet pressure was set as 10 kPa and 100 kPa, the cold end pressure was set as 0, and the hot exit pressure was set variable to imitate the different design pressures and cold mass fraction (CMF), the CMF is defined by:

$$\mathrm{CMF}=\frac{m_{\mathrm{c}}}{m_{i}} \tag{5}$$

where the m_{c} as the mass flow rate in the cold end, kg/s; m_{i} represents the total inlet mass flow rate, kg/s.

Table 4 Boundary conditions

Parameters	Type	Pressure/kPa	Temperature/K
inlet	Pressure inlet	100 10	293
cold end	Pressure outlet	0	293
hot exit	Pressure outlet	various	293
CMF	0.1~0.9 (interval of 0.1)	\	\

The schemes for solving equations were based on the finite volume approach, and residuals were set in the following way: 10^{-6} for continuity, *x*-velocity, *y*-velocity, *z*-velocity and energy; for κ–ε turbulence models and κ–ω turbulence models, the

residuals for κ and ε was 10^{-6}, for ω was 10^{-3}; for RSM turbulence model, the residuals for ω and six types stress were 10^{-3}, other solution methods were also showed in **Table 5**. In this study, a fine mesh was generated using ANSYS ICEM CFD. Considering that the second-order upwind difference scheme can more accurately capture the variations of physical quantities in the flow field and significantly improve the computational accuracy[13]., the second-order upwind difference scheme was employed for both the energy and momentum equations.

Table 5 Solution methods

Parameters	Type
solver	Pressure-Based, Absolute
time	Steady
scheme	SIMPLE
gradient	Least Squares Cell Based
pressure	Second Order
density	Second Order Upwind
momentum	Second Order Upwind
modified turbulent viscosity	Second Order Upwind
energy	Second Order Upwind

2.5 Validation of turbulence models

It is obvious and easy to measure in the complex flow structure of vortex tubes is axial velocity. As a result, the axial velocity in z direction (U_z) acquired by the numerical simulation with the six turbulence models were compared against experimental results[32] obtained by Laser Doppler Velocimetry under the inlet pressure P_{in}=10 kPa and the CMF=0.3 at six axial position of z=30 mm, z=60 mm, z=120 mm, z=180 mm, z=250 mm and z=330 mm in the main pipe is illustrated in **Fig. 3**.

Journal of Thermal Science and Engineering Applications. Received November 14, 2025;
Accepted manuscript posted March 31, 2026. doi:10.1115/1.4071557

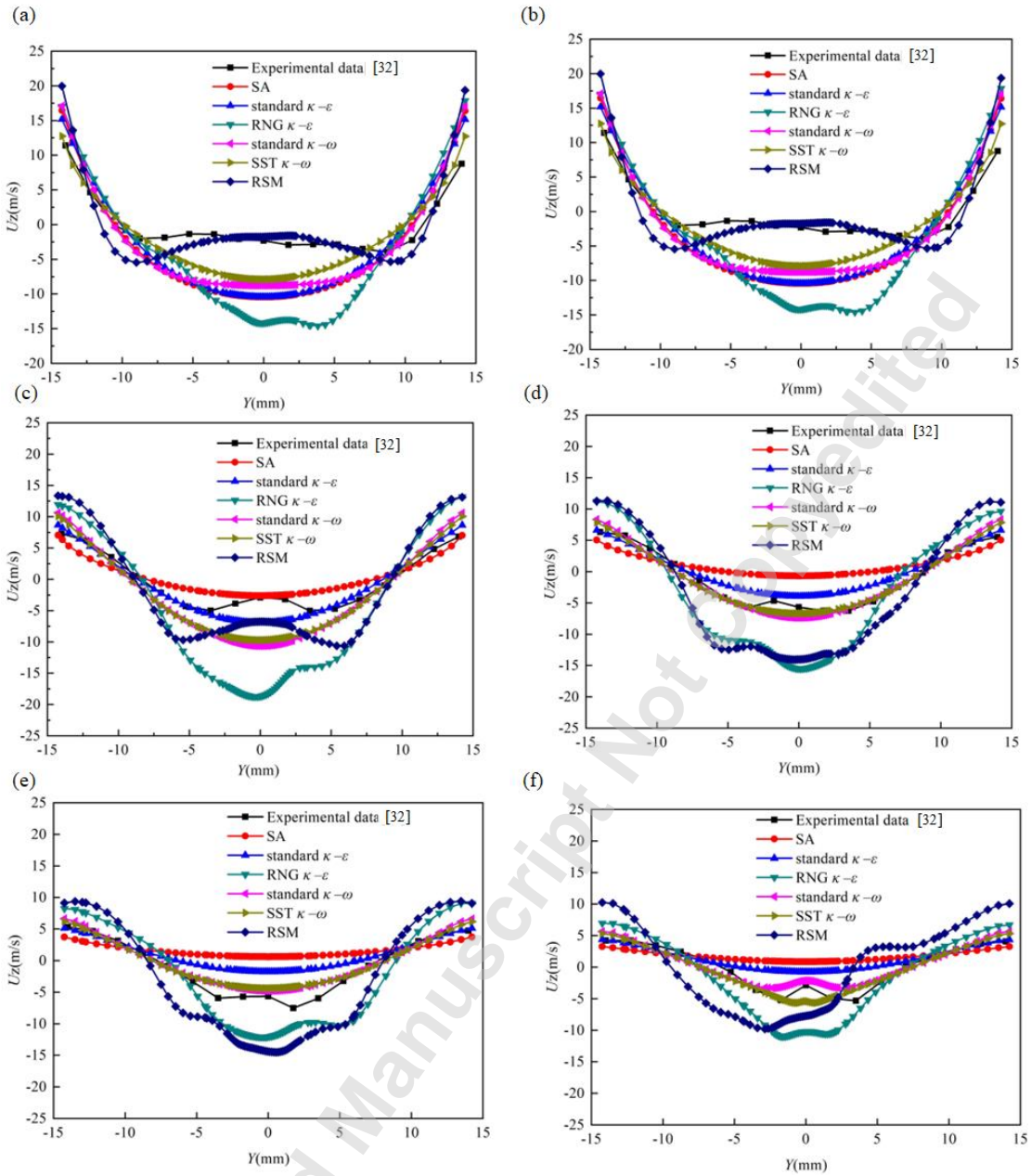

Fig. 3 The U_z distributions at different z position: (a) z=30 mm, (b) z= 60 mm, (c) z=120 mm, (d) z=180 mm, (e) z=250 mm, (f) z=330 mm

The deviation between the experimental results and the numerical simulation data obtained from RNG κ–ε model was large, so it was tough to describe the correct velocity field of the vortex tube. And the similar consequence was obtained by Dutta et al.[26], the RNG κ–ε turbulence model reveals laminar-like flow around the axis, and due to much lower turbulence viscosity values and insufficient mixing, the turbulence level of the entire main pipe is significantly reduced.

Compared to RNG κ–ε model, there is tinier difference between the numerical simulation data obtained with RSM model and the experimental results. Carefully, the

RSM model over-predicted the U_z in axis at z=30 mm and 60 mm but under-predicted the U_z in axis at z=120 mm. Near the axis of the vortex tube (-5 mm<z<5 mm), the numerical simulation data are closest to the experimental results. As the radial position increases, the deviation between the numerical simulation data and experimental results gradually increases, but the U_z variation trend in the Y direction of the entire vortex tube is basically consistent. As the axial position increases, the difference between the numerical simulation data obtained with RSM model and the experimental results increases, numerical simulation data acquired from RSM model no longer fit well with the experimental results at z>120 mm.

Even though they were certain difference in axis and wall position between experimental results and numerical simulation data obtained with SA, standard κ–ε, standard κ–ω and SST κ–ω models, the general trends agree with very well in -15 mm~-5 mm and 15 mm~5 mm at Y direction. The numerical simulation data acquired from above four turbulence models share some common trends at axis position, furthermore, the numerical simulation data obtained with standard κ–ω and SST κ–ω models were closer to the experimental results and the closest match provided by standard κ–ω model especially near the axis and walls.

Furthermore, a comparison was made between the ΔT obtained from simulation and experiment under the same working condition to explore the reliability of the 6 turbulence models, as shown in **Fig. 4**. From the comparison results, it can be seen that the ΔT obtained by 5 turbulence models and experiment presents a new increase followed by a decrease due to the increase of cold mass fraction, only the ΔT obtained by standard κ–ε model decreases due to the increase of cold mass fraction. Even if the ΔT trends obtained by these 5 models are in good with the experimental value, there is a significant difference in ΔT deviation between the simulated and experimental results. It can be clearly observed that standard κ–ω turbulence model has the smallest temperature deviation, with a minimum deviation of 1.5 K and a maximum deviation of only 3.3 K. This proves that the standard κ–ω turbulence model can better reflect the temperature separation inside the vortex tube. So, hereafter merely the standard κ–ω turbulence model was used for the numerical simulations and analysis.

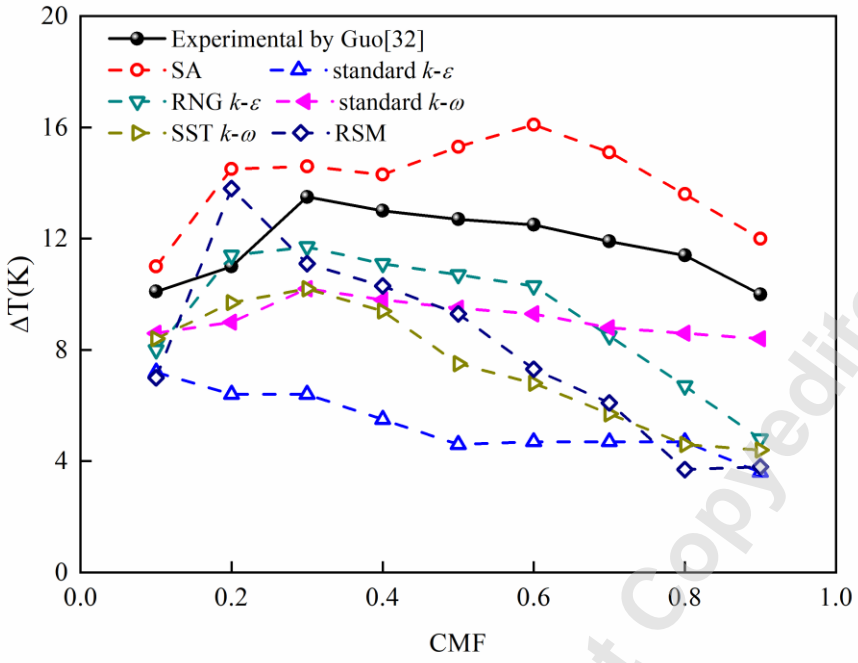

Fig. 4 The ΔT comparison of 6 turbulence models and experiment

3. Results and discussions

3.1 Total temperature distribution under different CMF

For the purpose of obtaining a clear temperature separation, in the following discussion, the temperature separation was analyzed at inlet pressure P_{in}=100 kPa, which has been proven to be a direct result of inlet pressure[1].

The total temperature distribution at various CMF in the vortex tube simulated by standard $\kappa-\omega$ turbulence model is given in **Fig. 5**. A temperature separation phenomenon is clearly demonstrated in the vortex tube, not only in the axial direction, but also in the radial direction. Cold end fluids are produced at the cold end, whereas hot exit fluids are produced at the hot end; cold fluids are located near the axis, while hot fluids gather in the peripheral region, and the temperature increases radially outwards across all cross sections in the radial direction. However, a large portion of the fluid can only exit from a single outlet (either the cold end or the hot exit) due to the control valve at the hot exit being opened too small or too large, there is no obvious

evidence of temperature separation in the radial direction when the CMF is very low (CMF=0.1) or high (CMF=0.9).

In the vortex tube, there is clearly a drop in temperature at the cold end, which is referred to as the cooling effect, and a rise in temperature at the hot exit, which is referred to as the heating effect. Furthermore, when CMF is 0.1 and 0.3, it is observed that the cold end exhibits the lowest temperature field, however the cold end also exhibits a local warm range (red dash circle) depicted in Fig. 5(a) and Fig. 5(b). When CMF=0.1, this warm range (red dash circle) even occupies almost the entire cold end, but when CMF=0.3, the local warm range nearly disappears. Meanwhile, a low-temperature area (black dash rectangle) appears at the hot exit in Fig. 5(b)~(e), and the low-temperature area (black dash rectangle) at the hot exit increases significantly when CMF is high. In the next section, we will examine the cooling effect and heating effect of the vortex tube, as well as the local warm spots at the cold end and the low-temperature region where the hot outlet appears.

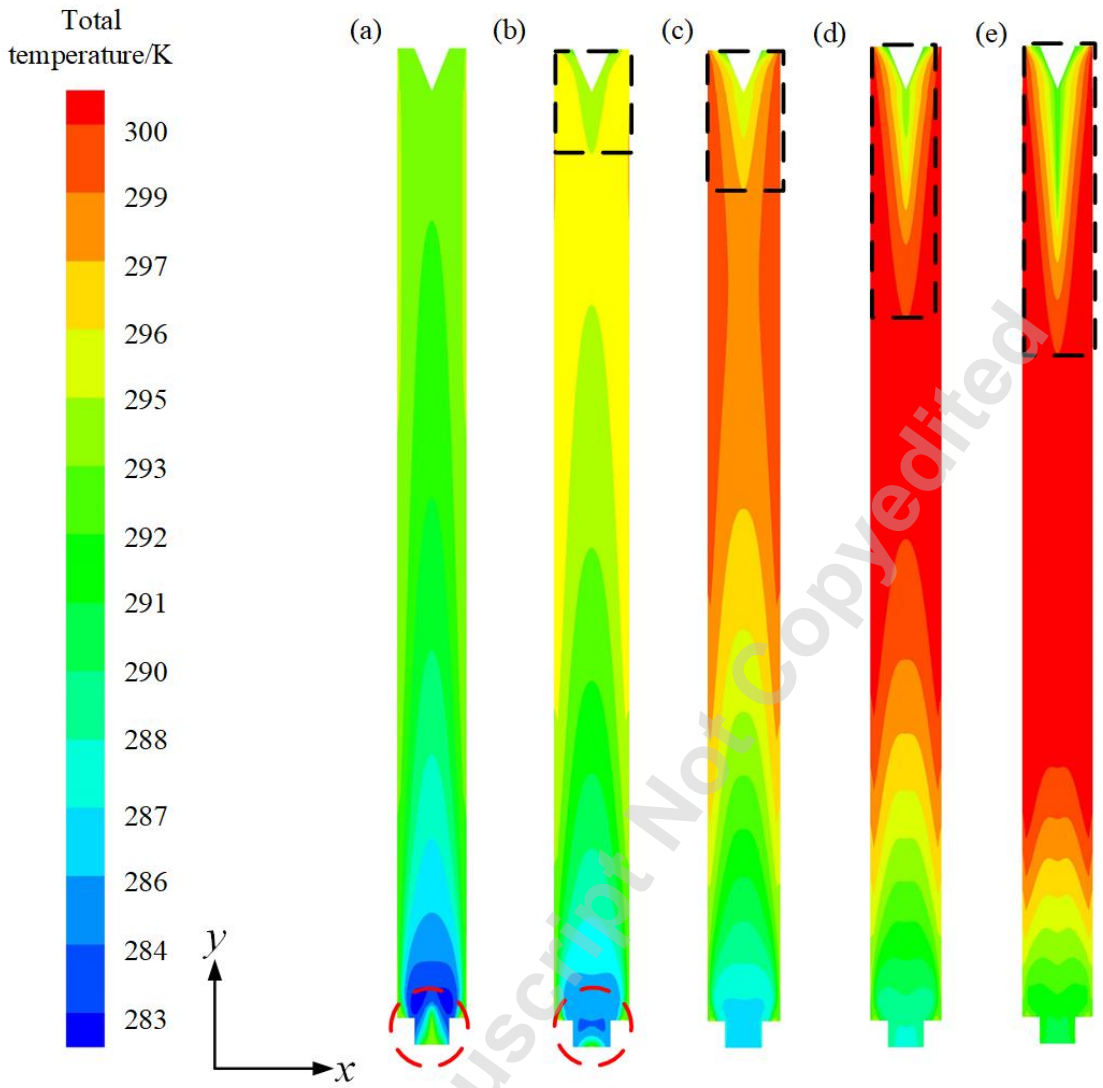

Fig. 5 Total temperature distribution under different CMF: (a): CMF=0.1; (b): CMF=0.3; (c): CMF=0.5; (d): CMF=0.7; (e): CMF=0.9

3.2 Cooling effect under different CMF

As shown in **Fig. 6**, the lowest temperature in the vortex tube increases linearly with the increase of the cold mass fraction, the mass flow rate discharged from the cold end is minimal when the cold mass fraction is low (CMF=0.1), which promotes a cooling effect from occurring. Meanwhile, the cold mass fraction is large (CMF=0.9), there is a substantial amount of mass flow discharged from the cold end, and the internal balance of the temperature separation in the vortex tube is disturbed. Which means that the cooling effect of the vortex tube should decrease with the increase of the cold mass

fraction. However, the vortex tube's cooling effect increases with increasing cold mass fraction, and then decreases as the cold mass fraction increases, the maximum cooling effect is obtained at CMF=0.5, and the cooling effect is almost axisymmetric (CMF=0.5 as the axis). This is because there is a temperature difference between the cold end average temperature and the lowest temperature in the vortex tube, the temperature difference between the cold end average temperature and the lowest temperature in the vortex tube is large in low cold mass fraction, and the temperature difference between the cold end average temperature and the lowest temperature in the vortex tube can be ignored when CMF≥0.5. This also can be proven in section 3.1 in Fig. 5(a) and Fig. 5(b), a local warm region (red dashed circle) exits the cold end when the cold mass fraction is less than 0.5. Leading to the cold end average temperature and cooling effect decreases first and then increases with the increase of the cold mass fraction.

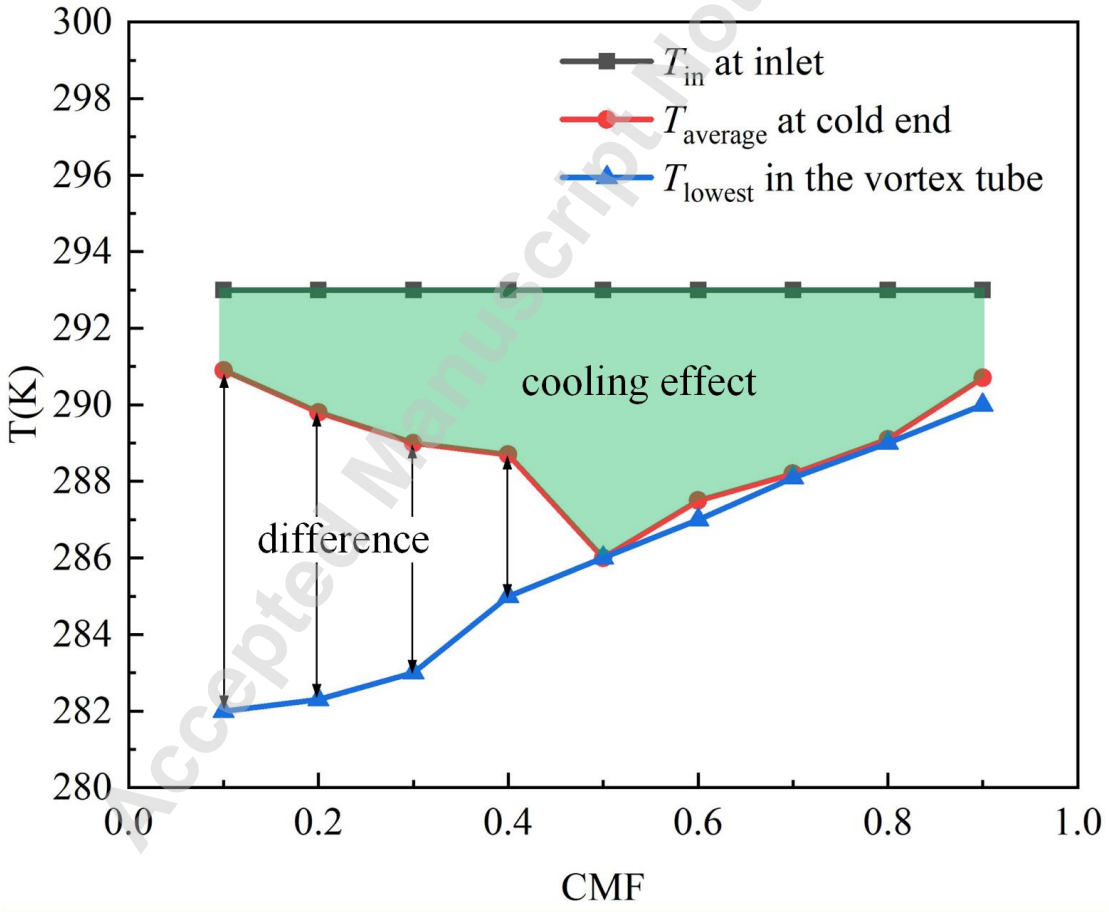

Fig. 6 Cooling effect and the distribution of cold end average temperature and the lowest temperature under different CMF

To explain this temperature difference phenomenon and cooling effect trend in the

cold end of the vortex tube, flow streamlines under various cold mass fractions were calculated and shown in Fig. 7.This shown clearly that the existence of a peripheral flow and an inner reverse flow in the vortex tube. The peripheral flow comes out from the hot exit and the reverse flow outflow from the cold end. The profiles also indicated the presence of secondary circulation flow near the inlet (pink dash circle) in **Fig. 7**. The formation of the secondary circulation flow near the inlet is due to the smaller exit aperture of the cold end compared to the reverse flow, which causes the backflow reverse flow to collide with the cold end wall[35] and the presence of secondary circulation flow enhances heat transfer[20]. From Fig. 7, we can see that the increase of the CMF lead to a decrease of the secondary circulation flow zone. Furthermore, backflow (red dashed circle) in the cold end is responsible for the temperature difference between the cold end average temperature and the lowest temperature in the vortex tube, as can be seen in Fig. 7(a). The backflow in the cold end is severe and occupies almost the entire cold end, restricting the temperature drop and the cooling effect of the vortex tube deeply when CMF=0.1. Since backflow in the cold end decreases, and this phenomenon can be observed visually (red dashed circle) in Fig. 7(a) and Fig. 7(b), the temperature difference decreases as the cold mass fraction increases. Small cold mass fractions do not allow the fluid to flow evenly through the cold end, resulting in some negative pressure regions in the cold end, where outside air (specified at 1 bar and 293 K in CFD setup) can flow into these negative pressure regions, as shown in Fig. 8, the same backflow has also been observed by previous CFD works[25].

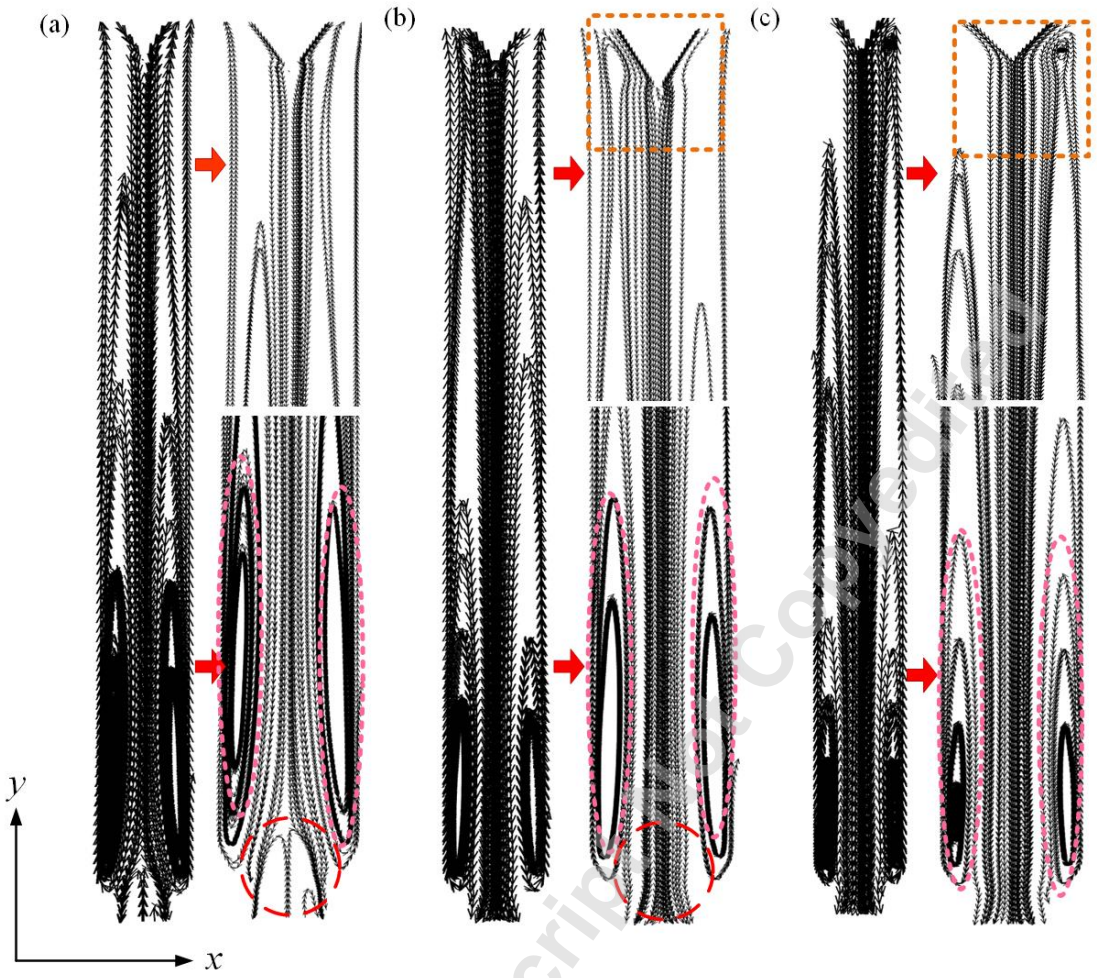

Fig. 7 Distribution of flow streamline at different CMF: (a): CMF=0.1; (b): CMF=0.5; (c): CMF=0.9

Fig. 8 provides an indication of the total pressure distribution in the cold end at varying cold mass fractions. In the cold end, there are large regions of negative pressure when CMF is 0.1 and CMF is 0.3, and the negative pressure area disappears immediately when CMF is 0.5. The generation and disappearance of negative pressure regions have a significant impact on backflow, which in turn affects the lowest and average temperatures in the cold end, leading to an increase and then decrease in cooling effect with the increase of cold mass fraction.

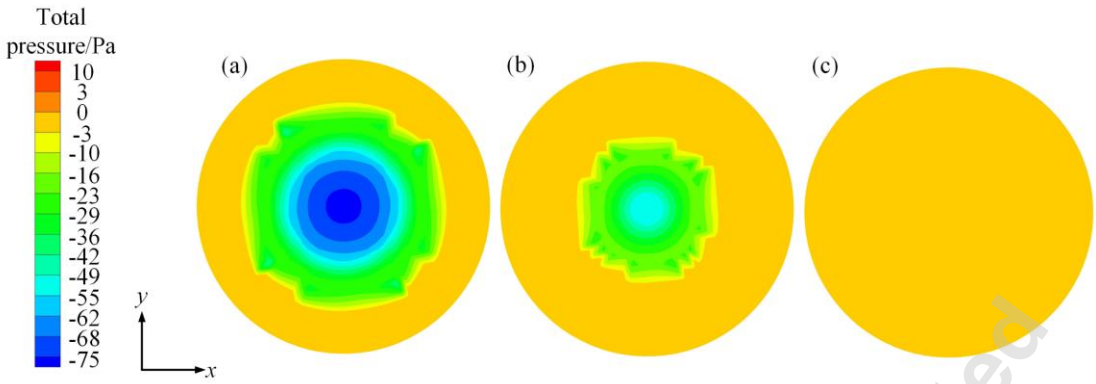

Fig. 8 Total pressure distribution on the cold end at different CMF: (a): CMF=0.1; (b): CMF=0.3; (c): CMF=0.5

Thus, there is a coupling effect between the cold mass fraction and the backflow on the cooling effect. Due to the presence of backflow in the cold end, the trend of cold mass fraction on cooling effect has been completely changed, indicating that the backflow in cold end has a greater impact on cooling effect than the cold mass fraction. In order to achieve better cooling effect of vortex tube, it is recommended to avoid the influence of cold end backflow as much as possible and set the appropriate cold mass fraction (CMF=0.3~0.7).

3.3 Heating effect under different CMF

As a result of the cooling effect involved in temperature separation, the vortex tube also generates heating effect, which is determined by the rise in temperature at the hot exit. **Fig. 9** illustrates the distribution of average temperature at the hot exit, the highest temperature in the vortex tube and heating effect at different CMF. The highest temperature in the vortex tube almost increases linearly with the increase of the cold mass fraction, while the hot exit average temperature and the vortex tube's heating effect increases slowly as the cold mass fraction increases. When the cold mass fraction is low (CMF=0.1), there is a massive amount of mass flowing out of the hot exit, and the internal balance of the temperature separation in the vortex tube is disturbed, resulting in poor heating performance. Under the energy separation effect of the vortex tube, the working fluid temperature at the hot exit increases with the increase of cold mass fraction, obtaining the highest temperature and heating effect when the cold mass

fraction is high (CMF=0.9). However, compared to the cooling effect of vortex tubes, the heating effect is significantly insufficient.

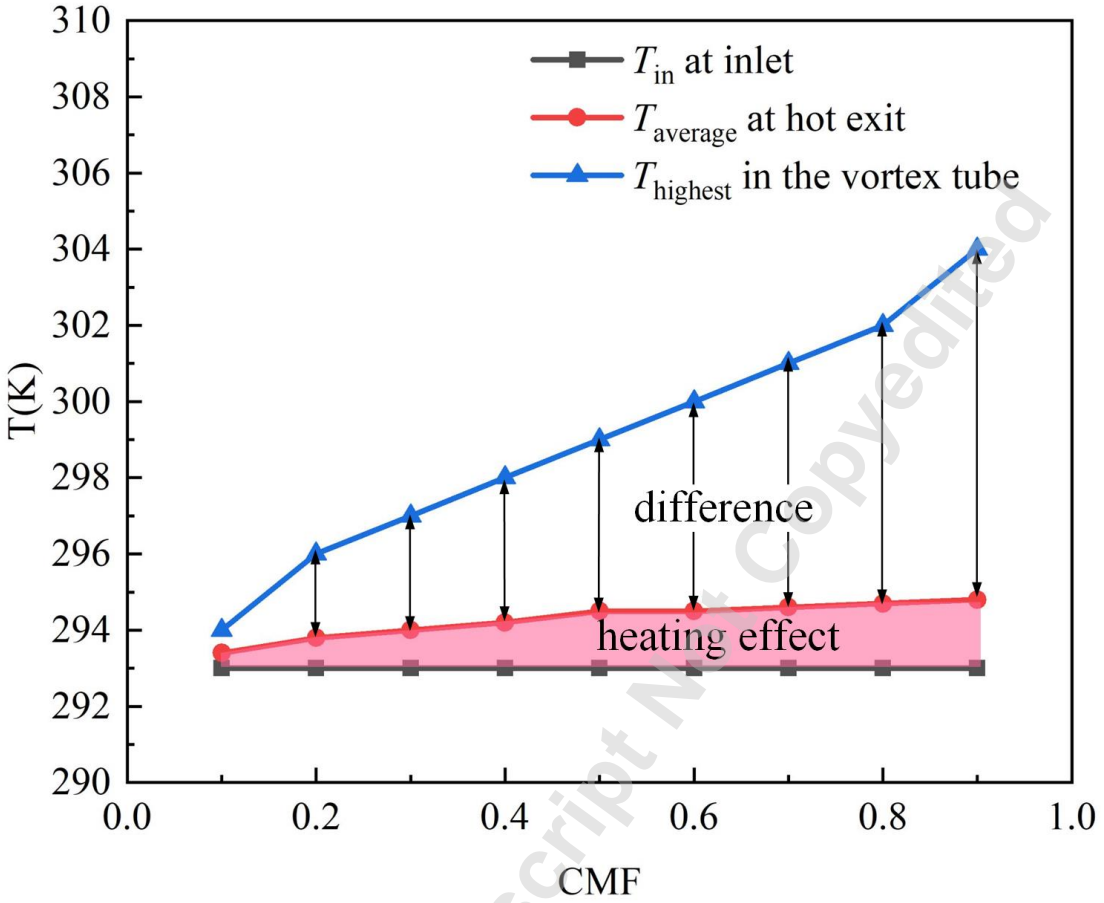

Fig. 9 Heating effect and the distribution of hot exit average temperature and the highest temperature under different CMF

Similarly, it can be seen from Fig. 9 that there is a large temperature difference between the hot exit average temperature and the highest temperature in the vortex tube, this phenomenon can also be qualitatively observed in in Fig. 5 (b)~(e), a local cold spots (black dash rectangle) are noted near the hot exit. Unlike the cooling effect, temperature difference does not change the trend of heating effect with the change of cold mass fraction. The heating effect continues to increase as the cold mass fraction. increases. However, the increase rate of the hot exit average temperature is much less the increase rate of the highest temperature in the vortex tube, the temperature difference between the hot exit average temperature and the highest temperature in the vortex tube becomes larger. This is because the backflow at hot exit (orange dash rectangle) as exemplified in the streamline plots as shown in Fig. 7(b) and Fig. 7 (c)

leading to the low-temperature regions as revealed in Fig. 5(c), Fig. 5 (d) and Fig. 5 (e). Moreover, as the cold mass fraction increases, the phenomenon of backflow at the hot exit becomes more pronounced, inducing a temperature difference between the hot exit average temperature and the highest temperature in the vortex tube, reducing its heating effect.

As a result of coupling between backflow at the hot exit and cold mass fraction, the heating effect slightly increases, indicating that even though hot exit backflow will always restrict heating effect, the cold mass fraction has a greater impact on heating effect.

In order to analyze backflow from hot exit, **Fig. 10** illustrates the distribution of reverse flow boundaries at various cold mass fractions. Since 360 mm is a short length, the reverse flow boundary reaches the control valve at CMF=0.1, and the diameter of the reverse flow boundary is less than the maximum cross section of the control valve, outside air never enters the vortex tube from the hot exit. A growing cold mass fraction enhances the adverse pressure gradient along the axis, which leads to the expansion of the reverse flow boundary. Due to tube length limitations, the reverse flow boundary cannot be extended axially but can only be expanded radially, resulting in a gradual increase in the diameter of the reverse flow boundary, which is even greater than the maximum cross section of the control valve, outside air even enters the vortex tube from the hot exit, as illustrated in Fig. 10(b)~(e). The above explanation is the cause of backflow at hot exit.

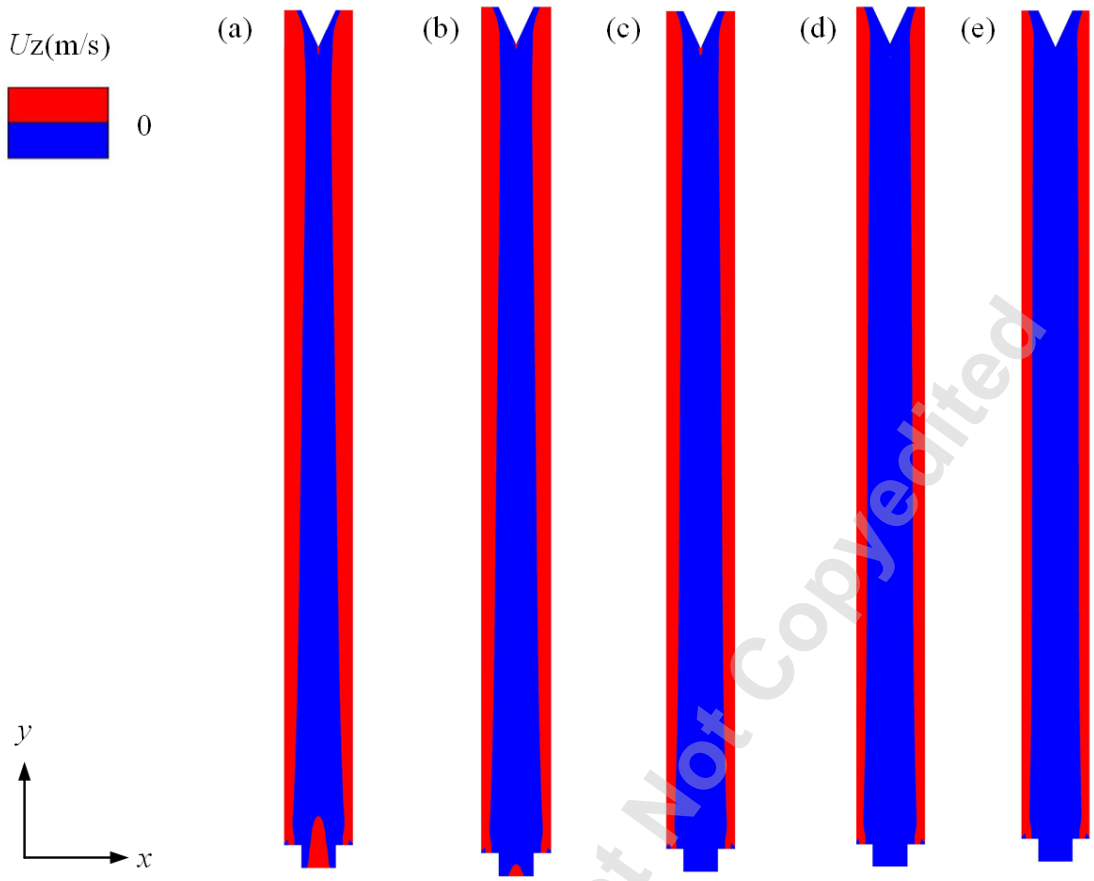

Fig. 10 The distribution of reverse flow boundary at different CMF; (a): CMF=0.1; (b): CMF=0.3; (c): CMF=0.5; (d): CMF=0.7; (e): CMF=0.9

In light of the above series of analysis, it is clear that cooling effect and heating effect are heavily limited by backflow in the cold end and hot exit, and backflow can even alter the trend of the cooling effect with respect to the cold mass fraction. And the mechanism of backflow of vortex tubes under different cold mass fraction has been analyzed. In the following section, the effect of backflow on the cooling effect and heating effect under different inlet pressures and DRs under CMF=0.3 will be discussed. The diameter of the main pipe (D_m) remains unchanged, while the diameter of the cold end (D_c) changes to obtain different DR.

3.4 Cooling effect and heating effect under different inlet pressure and DR

The distribution of cooling effect and heating effect at different inlet pressure is given in **Fig. 11**. The cooling effect of vortex tube will increase with the increase of

inlet pressure, and the heating effect is also the same. Similar to the influence of cold mass fraction on cooling effect and heating effect, under the same inlet pressure, the cooling effect of vortex tubes is much higher than their heating effect. Just like Fig. 6 and Fig. 9, the temperature difference between the cold end average temperature and the lowest temperature in the vortex tube and the distribution of the average temperature at the hot exit and the highest temperature in the vortex tube are caused by backflow and indicate its strength. An increase in temperature difference indicates that there was an increase in backflow at both the cold end and hot exit. It can be seen from Fig. 11 that when the inlet pressure is smaller than 100 kPa, the backflow in cold end and hot exit increases as the inlet pressure increases, whereas when the inlet pressure is larger than 100 kPa, the backflow in cold end and hot exit remains almost no longer affected by the inlet pressure. As a result, in order to achieve better cooling effect and heating effect of the vortex tube, the inlet pressure should be increased as much as possible.

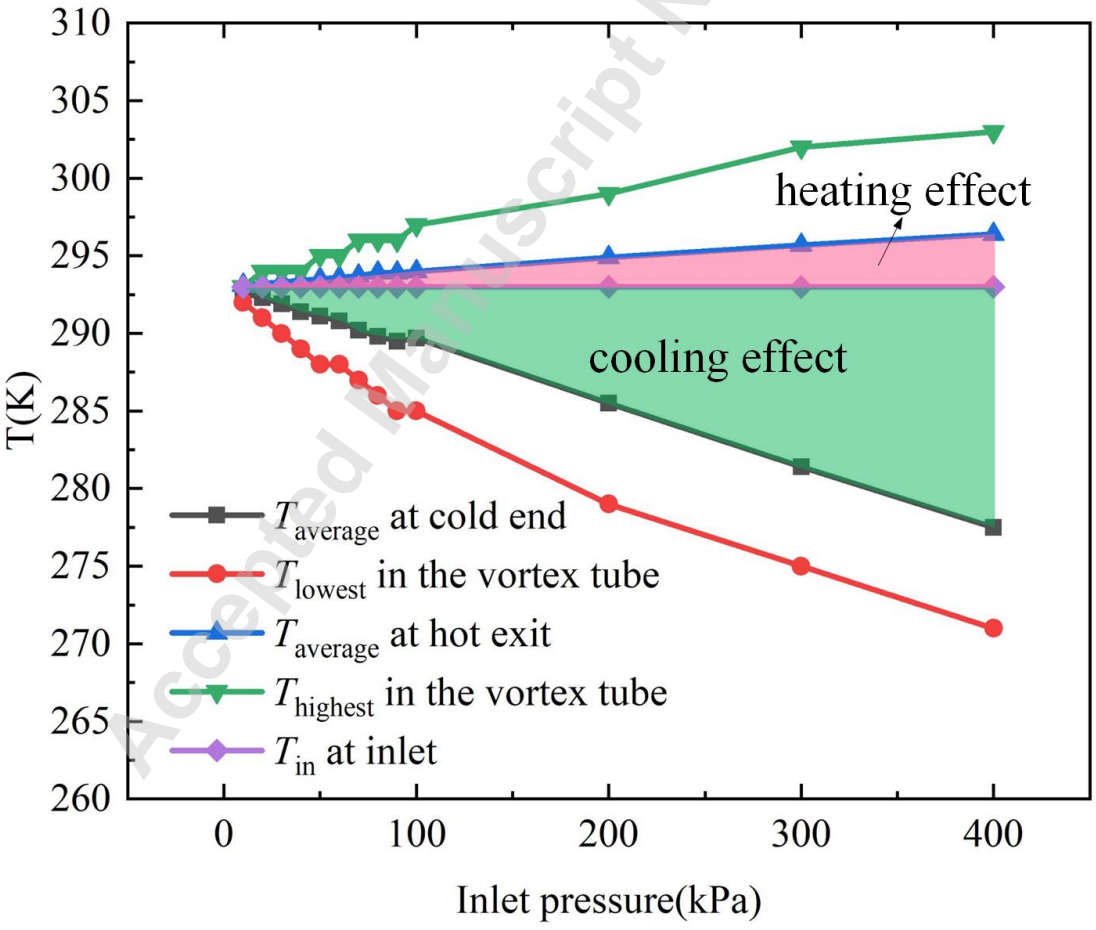

Fig. 11 Distribution of cooling effect and heating effect at different inlet pressure

The distribution of cooling effect and heating effect at different DR is given in **Fig.**

12. From this figure, it can be observed that, the cooling effect of the vortex tube gradually decreases with the increase of the diameter ratio, while the heating effect is basically not affected by the diameter ratio. Furthermore, with the increase of diameter ratio, the temperature difference between the cold end average temperature and the lowest temperature in the vortex gradually increases, indicating an intensification of cold end backflow, thus leading to a decrease in cooling effect. Under different diameter ratios, the effect of backflow on the hot end average temperature and the highest temperature in the vortex tube is also the same, but it does not significantly reduce the heating effect of the vortex tube. This indicates that under different diameter ratios, the influence of cold end backflow on the cooling effect is much stronger than that of hot end backflow on the heating effect. It should be design and use vortex tubes with small diameter ratios to achieve better cooling effect and heating effect.

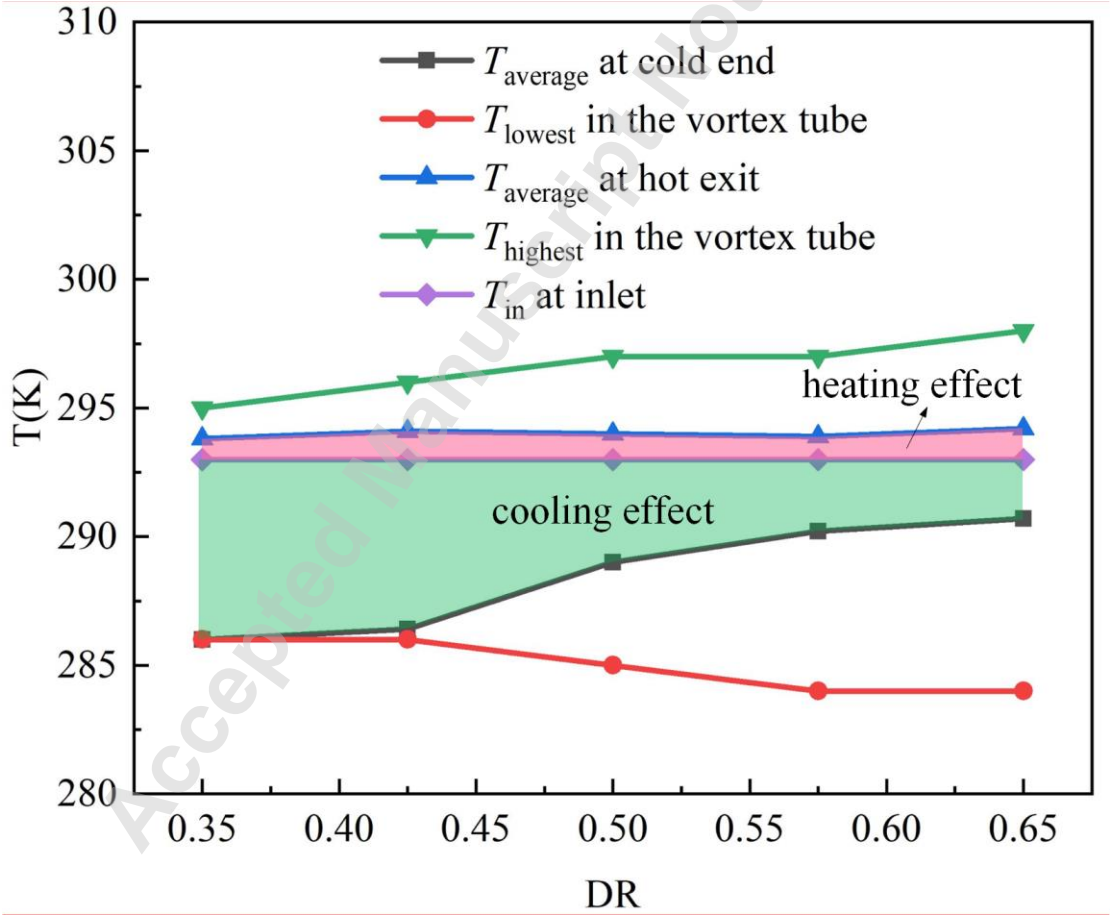

Fig. 12 Distribution of cooling effect and heating effect at different DR

4. Conclusion

Although abundant research in the vortex tube has been investigated, there still is little analysis of cooling effect and heating effect. A 3D computational model was developed and numerical simulations were conducted using six turbulence models. Firstly, the axial velocity obtained from the numerical simulation was compared with the experimental values to verify the reliability of the numerical simulation. Then, the cooling effect and heating effect under different cold mass fraction, inlet pressure and diameter ratio were investigated in this study. The main conclusions are as follows:

1. The numerical simulation results with six turbulence models were compared with experimental data on axial velocity. Predictions with the standard κ–ω model are best fit with experimental results were covered in this study, which providing guidance for the selection of turbulence models for numerical simulation of vortex tubes.
2. The cooling effect and heating effect of vortex tubes are suppressed by backflow under different CMF, even change the trend of the influence of CMF on the cooling effect.
3. Backflow at cold end caused by negative pressure often occur at low CMF, because it is difficult for the working fluid to flow out of the cold end, while backflow at hot exit occurs at high CMF, and the reverse flow boundary exceeds the control valve.
4. In order to get excellent cooling effect and heating effect of the vortex tube, the inlet pressure should be increased while reducing the diameter ratio of the vortex tube, and the CMF should be controlled within a reasonable range (CMF=0.3~0.7).

References

[1] P. Ambedkar, T. Dutta, Analysis of various separation characteristics of Ranque-Hilsch vortex tube and its applications – A review, Chem. Eng. Res. Des. 191 (2023) 93–108. https://doi.org/10.1016/j.cherd.2023.01.019.

[2] Z. Hu, R. Li, X. Yang, M. Yang, R. Day, H. Wu, Energy separation for Ranque-Hilsch vortex tube: A short review, Therm. Sci. Eng. Prog. 19 (2020) 100559.

https://doi.org/10.1016/j.tsep.2020.100559.

[3] W. Xu, Z. Yu, Q. Mu, B. Peng, Q. Li, Study of an integrated vortex tube used in hydrogen pre-cooling system, Int. J. Hydrog. Energy 54 (2024) 971–978. https://doi.org/10.1016/j.ijhydene.2023.11.122.

[4] Y. Li, G. Yan, Y. Yang, P. Dong, G. Liu, Thermodynamic analysis of new configurations of auto-cascade refrigeration cycles integrating the vortex tube, Energy 308 (2024) 132982. https://doi.org/10.1016/j.energy.2024.132982.

[5] A. Mansour, R. Oberti, H. Nesreddine, S. Poncet, Thermodynamic analysis of a transcritical CO 2 heat pump integrating a vortex tube, Appl. Therm. Eng. 224 (2023) 120076. https://doi.org/10.1016/j.applthermaleng.2023.120076.

[6] E.J. Kolmes, V.I. Geyko, N.J. Fisch, Heat pump model for Ranque–Hilsch vortex tubes, Int. J. Heat Mass Transf. 107 (2017) 771–777. https://doi.org/10.1016/j.ijheatmasstransfer.2016.11.072.

[7] M. Senturk Acar, O. Arslan, Exergo-economic Evaluation of a new drying system Boosted by Ranque-Hilsch vortex tube, Appl. Therm. Eng. 124 (2017) 1–16. https://doi.org/10.1016/j.applthermaleng.2017.06.010.

[8] A.N. Shmroukh, A. Radwan, A. Abdal-hay, A.A. Serageldin, M. Nasr, New configurations for sea water desalination system using Ranque-Hilsch vortex tubes, Appl. Therm. Eng. 157 (2019) 113757. https://doi.org/10.1016/j.applthermaleng.2019.113757.

[9] S.E. Rafiee, M.M. Sadeghiazad, N. Mostafavinia, Experimental and Numerical Investigation on Effect of Convergent Angle and Cold Orifice Diameter on Thermal Performance of Convergent Vortex Tube, ASME J. Therm. Sci. Eng. Appl. 7 (2015). https://doi.org/10.1115/1.4030639.

[10] M.N. Fuqua, J.L. Rutledge, Experimental Investigation of Ranque–Hilsch Vortex Tube Performance Characteristics with High-Temperature Air, ASME J. Therm. Sci. Eng. Appl. 17 (2025). https://doi.org/10.1115/1.4069038.

[11] M.N. Fuqua, J.L. Rutledge, Computational Investigation of the Operating Mechanism of the Ranque–Hilsch Vortex Tube, ASME J. Therm. Sci. Eng. Appl. 17 (2024). https://doi.org/10.1115/1.4066984.

[12] M.N. Fuqua, J.L. Rutledge, An Experimental and Computational Investigation of Ranque–Hilsch Vortex Tube Heat Transfer Characteristics, ASME J. Therm. Sci. Eng. Appl. 16 (2023). https://doi.org/10.1115/1.4063826.

[13] R.K. Singh, A.K. Pramanick, S.C. Rana, Numerical Analysis of Temperature Separation and Exergy Analysis of a Dual-Inlet Section Convergent Vortex Tube, ASME J. Therm. Sci. Eng. Appl. 15 (2023). https://doi.org/10.1115/1.4062314.

[14] S. Syed, M. Renganathan, Numerical investigations on flow characteristics and energy separation in a Ranque Hilsch vortex tube with hydrogen as working medium, Int. J. Hydrog. Energy 44 (2019) 27825–27842. https://doi.org/10.1016/j.ijhydene.2019.08.239.

[15] H. Yan, Q. Xu, Y. Zhao, Y. Xue, The thermal performance of a novel convergent valveless vortex tube, Int. J. Refrig. 119 (2020) 92–101. https://doi.org/10.1016/j.ijrefrig.2020.07.007.

[16] F. Liang, Q. Zeng, G. Tang, L. Xin, Q. Li, N. Li, Numerical investigation on the effect of convergent-divergent tube on energy separation characteristic of vortex tube, Int. Commun. Heat Mass Transf. 133 (2022) 105927. https://doi.org/10.1016/j.icheatmasstransfer.2022.105927.

[17] R. Shamsoddini, A. Faghih Khorasani, A new approach to study and optimize cooling performance of a Ranque–Hilsch vortex tube, Int. J. Refrig. 35 (2012) 2339–2348. https://doi.org/10.1016/j.ijrefrig.2012.08.022.

[18] N. Bej, K.P. Sinhamahapatra, Exergy analysis of a hot cascade type Ranque-Hilsch vortex tube using turbulence model, Int. J. Refrig. 45 (2014) 13–24. https://doi.org/10.1016/j.ijrefrig.2014.05.020.

[19] H.R. Thakare, A.D. Parekh, CFD analysis of energy separation of vortex tube employing different gases, turbulence models and discretisation schemes, Int. J. Heat Mass Transf. 78 (2014) 360–370. https://doi.org/10.1016/j.ijheatmasstransfer.2014.06.083.

[20] V. Bianco, A. Khait, A. Noskov, V. Alekhin, A comparison of the application of RSM and LES turbulence models in the numerical simulation of thermal and flow patterns in a double-circuit Ranque-Hilsch vortex tube, Appl. Therm. Eng. 106 (2016)

1244–1256. https://doi.org/10.1016/j.applthermaleng.2016.06.095.

[21] M. Baghdad, A. Ouadha, O. Imine, Y. Addad, Numerical study of energy separation in a vortex tube with different RANS models, Int. J. Therm. Sci. 50 (2011) 2377–2385. https://doi.org/10.1016/j.ijthermalsci.2011.07.011.

[22] X. Liu, Z. Liu, Investigation of the energy separation effect and flow mechanism inside a vortex tube, Appl. Therm. Eng. 67 (2014) 494–506. https://doi.org/10.1016/j.applthermaleng.2014.03.071.

[23] O.A.A. Awan, R. Sager, L. Pehle, M. Wirsum, E. Juntasaro, Three dimensional numerical analysis of the performance of different working fluids in vortex tubes, Appl. Therm. Eng. 261 (2025) 125130. https://doi.org/10.1016/j.applthermaleng.2024.125130.

[24] K. Shaji, K.-K. Lee, F. Salmani, H.D. Kim, Numerical analysis and an approach for optimization of the Ranque–Hilsch vortex tube for a compressible flow, Appl. Therm. Eng. 243 (2024) 122590. https://doi.org/10.1016/j.applthermaleng.2024.122590.

[25] Z. Wang, K.O. Suen, Numerical comparisons of the thermal behaviour of air and refrigerants in the vortex tube, Appl. Therm. Eng. 164 (2020) 114515. https://doi.org/10.1016/j.applthermaleng.2019.114515.

[26] T. Dutta, K.P. Sinhamahapatra, S.S. Bandyopdhyay, Comparison of different turbulence models in predicting the temperature separation in a Ranque–Hilsch vortex tube, Int. J. Refrig. 33 (2010) 783–792. https://doi.org/10.1016/j.ijrefrig.2009.12.014.

[27] Z. Hu, X. Zheng, F. Gao, H. Wu, Experimental and numerical investigation of rectifier designs for enhancing energy separation efficiency in vortex tubes, Appl. Therm. Eng. 272 (2025) 126389. https://doi.org/10.1016/j.applthermaleng.2025.126389.

[28] G. Tang, F. Liang, Z. Ma, Z. Wang, J. Chen, Y. Zhu, M. Jin, Investigation of cold tube structure on flow characteristics and energy separation in vortex tube based on numerical and thermodynamic analyses, Appl. Therm. Eng. 254 (2024) 123893. https://doi.org/10.1016/j.applthermaleng.2024.123893.

[29] W. Chen, Z. Luo, X. Li, S. Lu, F. Guo, Numerical study of temperature separation

characteristics of vortex tubes: Effects of structural parameters and modeling of cooling performance correlations, Therm. Sci. Eng. Prog. 39 (2023) 101715. https://doi.org/10.1016/j.tsep.2023.101715.

[30] F. Liang, G. Tang, H. Cui, M. Li, R. Ding, R. Guan, Z. Ma, Numerical analyses of the swirling flow characteristic and energy separation mechanism of hydrogen-mixed natural gas in the Ranque–Hilsch vortex tube, Int. J. Therm. Sci. 219 (2026) 110267. https://doi.org/10.1016/j.ijthermalsci.2025.110267.

[31] R. Oberti, J. Lagrandeur, S. Poncet, Numerical benchmark of a Ranque–Hilsch vortex tube working with subcritical carbon dioxide, Energy 263 (2023) 125793. https://doi.org/10.1016/j.energy.2022.125793.

[32] X. Guo, B. Zhang, L. Li, B. Liu, T. Fu, Experimental investigation of flow structure and energy separation of Ranque–Hilsch vortex tube with LDV measurement, Int. J. Refrig. 101 (2019) 106–116. https://doi.org/10.1016/j.ijrefrig.2019.02.004.

[33] Y. Xue, M. Arjomandi, R. Kelso, Energy analysis within a vortex tube, Exp. Therm. Fluid Sci. 52 (2014) 139–145. https://doi.org/10.1016/j.expthermflusci.2013.09.004.

[34] A. Bazgir, N. Nabhani, S. Eiamsa-ard, Numerical analysis of flow and thermal patterns in a double-pipe Ranque-Hilsch vortex tube: Influence of cooling a hot-tube, Appl. Therm. Eng. 144 (2018) 181–208. https://doi.org/10.1016/j.applthermaleng.2018.08.043.

[35] U. Behera, P.J. Paul, S. Kasthurirengan, R. Karunanithi, S.N. Ram, K. Dinesh, S. Jacob, CFD analysis and experimental investigations towards optimizing the parameters of Ranque–Hilsch vortex tube, Int. J. Heat Mass Transf. 48 (2005) 1961–1973. https://doi.org/10.1016/j.ijheatmasstransfer.2004.12.046.

Journal of Thermal Science and Engineering Applications. Received November 14, 2025;
Accepted manuscript posted March 31, 2026. doi:10.1115/1.4071557